Radiology

Early-Stage Non–Small Cell Lung Cancer: Quantitative Imaging Characteristics of ^{18}F Fluorodeoxyglucose PET/CT Allow Prediction of Distant Metastasis[1]

Jia Wu, PhD
Todd Aguilera, MD, PhD
David Shultz, MD, PhD
Madhu Gudur, PhD
Daniel L. Rubin, MD, MS
Billy W. Loo, Jr, MD, PhD
Maximilian Diehn, MD, PhD
Ruijiang Li, PhD

Purpose: To identify quantitative imaging biomarkers at fluorine 18 (^{18}F) positron emission tomography (PET) for predicting distant metastasis in patients with early-stage non–small cell lung cancer (NSCLC).

Materials and Methods: In this institutional review board–approved HIPAA-compliant retrospective study, the pretreatment ^{18}F fluorodeoxyglucose PET images in 101 patients treated with stereotactic ablative radiation therapy from 2005 to 2013 were analyzed. Data for 70 patients who were treated before 2011 were used for discovery purposes, while data from the remaining 31 patients were used for independent validation. Quantitative PET imaging characteristics including statistical, histogram-related, morphologic, and texture features were analyzed, from which 35 nonredundant and robust features were further evaluated. Cox proportional hazards regression model coupled with the least absolute shrinkage and selection operator was used to predict distant metastasis. Whether histologic type provided complementary value to imaging by combining both in a single prognostic model was also assessed.

Results: The optimal prognostic model included two image features that allowed quantification of intratumor heterogeneity and peak standardized uptake value. In the independent validation cohort, this model showed a concordance index of 0.71, which was higher than those of the maximum standardized uptake value and tumor volume, with concordance indexes of 0.67 and 0.64, respectively. The prognostic model also allowed separation of groups with low and high risk for developing distant metastasis (hazard ratio, 4.8; *P* = .0498, log-rank test), which compared favorably with maximum standardized uptake value and tumor volume (hazard ratio, 1.5 and 2.0, respectively; *P* = .73 and 0.54, log-rank test, respectively). When combined with histologic types, the prognostic power was further improved (hazard ratio, 6.9; *P* = .0289, log-rank test; and concordance index, 0.80).

Conclusion: PET imaging characteristics associated with distant metastasis that could potentially help practitioners to tailor appropriate therapy for individual patients with early-stage NSCLC were identified.

©RSNA, 2016

Online supplemental material is available for this article.

Non–small cell lung cancer (NSCLC) is the leading cause of cancer-related death worldwide. Stereotactic ablative radiation therapy (SABR), also known as stereotactic body radiation therapy, achieves excellent local control rates in patients with early-stage NSCLC (1). The dominant pattern of treatment failure in patients treated with SABR is distant metastasis (2). Therefore, there is a critical need to identify patients who are more likely to develop metastatic disease and who thus might benefit from additional therapy. This is pertinent with both surgical and SABR treatment, but more so with SABR, because lymph nodes are rarely evaluated pathologically before or after radiation.

Imaging with fluorine 18 (^{18}F) fluorodeoxyglucose (FDG) positron emission tomography (PET) is a well-established tool in staging NSCLC, because it allows detection of distant metastases and regional lymph nodes involved (3). Conventional PET imaging metrics such as peak standardized uptake value (SUV_{peak}), maximum SUV (SUV_{max}), and total lesion glycolysis have been shown to be useful prognostic indicators of survival in patients with NSCLC (4–6). Authors of multiple studies (7–9) have demonstrated that metabolic tumor volume is a prognostic factor in patients with NSCLC. However, despite intensive investigation of these and other imaging metrics, the predictive value of these metrics to allow accurate discrimination between different risk groups appears to be limited. More sophisticated tools that improve on existing imaging metrics are needed.

Radiomics has emerged as a promising approach to discovering quantitative imaging biomarkers in patients with cancer (10). The rationale is that, by extracting a large number of putative imaging features, we could obtain a more comprehensive characterization of the underlying tumor phenotypes, which may ultimately correlate with clinical outcomes. This approach has been used to predict overall survival in patients with lung cancer with widely available imaging data such as CT (11,12) or FDG PET (13,14).

We hypothesize that automated analysis of quantitative imaging features coupled with appropriate statistical modeling may lead to improved prognostic value compared with that of conventional imaging metrics. Here, we adopt a quantitative radiomic approach to extract imaging features from pretreatment FDG PET scans. The purpose of this study was to identify quantitative imaging biomarkers from FDG PET for predicting distant metastasis in patients with early-stage NSCLC.

Materials and Methods

Patient Population

Under approval from the institutional review board, we retrospectively reviewed records and images of patients with lung cancer (n = 449) who were treated with SABR at our institution from September 2005 through December 2013. Inclusion criteria were biopsy-confirmed primary NSCLC, stage I according to the sixth edition of the American Joint Committee on Cancer staging manual, with a minimum of 3 months of imaging follow-up (n = 197). A majority (> 80%) of patients were not eligible for surgery due to comorbidities such as advanced age, poor performance status, chronic obstructive pulmonary disease, coronary artery disease, pulmonary hypertension, liver cirrhosis, and poor lung function; some patients (< 20%) declined surgery. Exclusion criteria were treatment with concurrent chemotherapy before a diagnosis of distant metastasis (n = 16), synchronous tumors (n = 10), diagnosis with new primary NSCLCs after SABR (n = 5), and previous treatment for NSCLC (n = 31). On the bases of the inclusion and exclusion criteria, 135 patients were selected. Of those, 101 patients with pretreatment PET images available were included in this retrospective study.

Patient characteristics are summarized in Table 1. There was no

Advances in Knowledge

- The proposed median imaging signature was 0.83 (interquartile range, 0.69–1.15) for patients without distant metastasis, and was 1.29 (interquartile range, 0.80–1.80) for patients with distant metastasis (P = .02, Wilcoxon test).

- In an independent validation cohort, the PET radiomic signature achieved a concordance index of 0.71 in predicting distant metastasis, with a significant separation between high-risk and low-risk patients (hazard ratio, 4.8; P = .0498; log-rank test).

- When combined with histologic information, the prognostic power was further improved, with a concordance index of 0.80 in the validation cohort (hazard ratio, 6.9; P = .0289, log-rank test).

Implication for Patient Care

- Imaging signatures based on fluorine 18 fluorodeoxyglucose PET could potentially be used to identify early-stage lung cancer patients who might benefit from adjuvant systemic therapy.

Table 1

Demographic Data

Characteristic	Overall (n = 101)	Discovery (n = 70)	Validation (n = 31)	P Value
Age (y)*	75 (42–92)	77 (42–92)	71 (47–89)	.09
Sex				.46
Female	56 (55)	41 (59)	15 (48)	
Male	45 (45)	29 (41)	16 (52)	
Age*				
Men (y)	71 (55–89)	72 (55–89)	69 (59–89)	.43
Women (y)	78 (42–92)	78 (42–92)	74 (47–87)	.19
Overall stage				>.99
IA	70 (69)	48 (69)	22 (71)	
IB	31 (31)	22 (31)	9 (29)	
TNM stage				.50
T1	72 (71)	48 (69)	24 (77)	
T2a	29 (29)	22 (31)	7 (23)	
Histologic result				.05
Adeno	60 (59)	37 (53)	23 (74)	
Squamous	30 (30)	25 (36)	5 (16)	
Unknown	11 (11)	8 (11)	3 (10)	
Follow-up (mo)*	17 (2–80)	22.5 (2–80)	14 (2–29)	.02
Survival (mo)*	20 (3–80)	23 (3–80)	17 (6–40)	.04
Distant metastasis				>.99
No	85 (84)	59 (84)	26 (84)	
Yes	16 (16)	11 (16)	5 (16)	
Overall survival				.01
No	37 (37)	32 (46)	5 (16)	
Yes	64 (63)	38 (54)	26 (84)	
Time to distant metastasis (mo)*	8 (1–30)	8 (3–15)	9 (1–30)	.73

Note.—Unless otherwise indicated, data are number of patients, with percentage in parentheses. Statistical comparison between two cohorts was computed with χ^2 (categorical variables) or Wilcoxon rank sum test (continuous variables). TNM = tumor, node, and metastasis.

* Data in parentheses are the range.

statistically significant difference in age between the men and women ($P = .079$, Wilcoxon test). In the study cohort, 16 (15.8%) patients had distant metastasis during follow-up: adenocarcinoma ($n = 9$), squamous cell carcinoma ($n = 3$), and unknown histologic type ($n = 4$). These 16 patients had metastases to the thorax ($n = 11$), bone ($n = 5$), visceral organs ($n = 4$), and brain ($n = 2$). Note that some patients presented with multiple metastatic sites. Among them, metastatic disease was confirmed on the basis of biopsy results in seven patients and with PET imaging only in eight patients because of poor health condition and inability to undergo biopsy, and brain metastasis in one patient was confirmed with magnetic resonance imaging. At our institution, we follow up with all patients with NSCLC at regular intervals (usually every 3 months) after treatment. This process lasts indefinitely until patient death, unless they are lost to follow-up.

We divided the overall population into two independent cohorts. The first cohort, consisting of approximately two-thirds of the population, included patients imaged before the end of 2011 and was used for discovery or training purposes ($n = 70$). The second cohort included patients imaged between 2012 and 2013 and was used for validation purposes ($n = 31$). We chose the particular time frame to ensure a sufficiently large population size to build reliable prognostic models, and at the same time, achieved an equal distribution of events between the two cohorts (distant metastasis rate, 16%). Wilcoxon rank-sum and χ^2 tests were used to assess the differences between the two cohorts. The clinical end points evaluated in this study, including distant metastasis rate and time to distant metastasis, tended to have a similar distribution in both cohorts.

Treatment

Patients were treated with SABR within a week of treatment-planning PET/computed tomography (CT) scans. Radiation doses ranged from 25 Gy in a single fraction to 60 Gy divided into five fractions. The majority of patients (65%) received doses greater than the biologically effective dose of 100 Gy.

PET/CT Imaging

For NSCLC treated with SABR at our institution, patients routinely undergo PET/CT as part of initial staging and during radiation treatment simulation. Regarding the imaging protocol, after a 4–8-hour fast, patients were injected with 370–666 MBq of FDG, and imaging was performed 45–60 minutes later with a PET/CT scanner (GE Discovery; GE Medical Systems, Milwaukee, Wis, or Somatom; Siemens Healthcare, Erlangen, Germany). CT images were collected in the helical acquisition mode. In the same scanning locations and generally in seven bed positions, PET data were acquired in two-dimensional mode, with 3–5 minutes of acquisition time per bed position. The PET images were then reconstructed with an ordered set expectation maximization algorithm, with the CT data for attenuation correction. The complete PET/CT examination required approximately 1.5 hour, including patient setup, tracer uptake, and image acquisition. Most of the original PET image spatial resolution was $2.34 \times 2.34 \times 3.27$ mm^3, with in-plane resolution of 1.68–5.47 mm and thickness of 2.03–4 mm.

Image Feature Extraction

We calculated a total of 70 quantitative features from each patient's PET image to characterize intratumor heterogeneity and complexity. Our hypothesis was that these quantitative imaging

Table 2

Quantitative PET Image Characteristics for the Primary Tumor

Type	Details	No.
Morphology	Volume, sphericity	2
Statistical	Mean, max, standard deviation, uniformity, entropy, energy	6
Histogram	SUV defined with highly active metabolic tumor volume of 1–5 mL, with interval of 1 mL	5
GLCM	Compute co-occurrence matrices with offset of 1 for all 13 directions; average co-occurrence matrices throughout 13 directions; compute three features, including homogeneity, cluster shade, and correlation.	3
Wavelet	Apply one-level discrete wavelet decomposition; group the decomposed image into four rotational invariant groups: group 1 with HHH; group 2 with LLL; group 3 with LHH, HLH, HHL; and group 4 with LLH, LHL, HLL; process the group-wise averaged images with three statistical features (ie, mean, max and entropy) and three features.	24
Laws family	Apply each Laws filter consistently for all three directions, including Gaussian, gradient, LOG, Gabor, and wave filters; process the filtered image with three statistical features (ie, mean, max, and entropy) and three GLCM features.	30

Note.—H = high-pass filter, L = low-pass filter (eg, HHH = high-pass filter in three directions, LHL = one high-pass filter and two low-pass filters in three dimensions). GLCM = gray-level co-occurence matrix.

features may reveal subtle characteristics of the tumor that are otherwise not detectable (ie, by human eyes) and these imaging features provide a more comprehensive characterization of the underlying tumor phenotypes and may better predict clinical outcomes. The feature pool included two morphologic features, six statistical features, five histogram-related features, and 57 texture features, which are summarized in Table 2. In this work, we investigated three types of texture features on the basis of gray-level co-occurrence matrices (15), wavelet decompositions (16), and Laws features (17). To characterize tumors meaningfully, all texture features were further processed to be rotationally invariant (without preference to any particular spatial direction). The calculation of all imaging features was implemented with software (MATLAB; MathWorks, Natick, Mass).

Feature Selection

Because of the large number of image features and relatively small cohort size, we performed feature selection in three stages to minimize multiple hypothesis testing and avoid model over-fitting. First, we tested the reproducibility and stability of each imaging feature, given the uncertainty associated with tumor delineation. In particular, we derived two sets of imaging features on the basis of two sets of tumor contours based on a manual delineation by an experienced radiation oncologist and automatic segmentation with a fuzzy c-means algorithm (18). We kept only the most stable imaging features with an intraclass correlation coefficient greater than 0.8. Then we removed redundant imaging features with a linear correlation coefficient greater than 0.95. Finally, we applied the least absolute shrinkage and selection operator algorithm (19) jointly with the Cox survival model described in the next section, to implement a nested feature selection scheme in the discovery cohort. Ten-fold cross-validation was applied to minimize the potential selection bias, and the most frequently selected imaging features (with a cutoff of 0.05) were chosen to fit the final prediction model. The feature selection procedure was performed by using a statistical software package (glmnet package in R; R Foundation for Statistical Computing, Vienna, Austria [20]).

Prediction of Distant Metastasis

The Cox proportional hazards model (21) was used to build survival models to predict freedom from distant metastasis on the basis of the discovery cohort. In general, a Cox regression model is used to estimate the hazard or risk of a certain outcome or event (in this study, distant metastasis) for each patient. Ideally, all patients who had distant metastasis are associated a higher risk according to a perfect prediction model. Given the disparate follow-up times for different patients, a Cox survival model (as opposed to binary classification) is appropriate, because it takes into account the presence or absence of distant metastasis and the time to event. Since imaging and histologic evaluation measure the same biologic entity but at very different spatial scales, we assessed whether histologic type (adenocarcinoma vs squamous cell carcinoma) provided complementary value to imaging signatures by combining the two in a single prognostic model. To divide the patients into high- versus low-risk groups, we determined the optimal threshold value on the basis of the discovery cohort, which is defined as the cutoff point with the most significant split (smallest P value from the log-rank test) (22). The Cox survival model was built by using the survival package in R (23).

Performance Evaluation and Statistical Analysis

We validated the prediction model in an independent validation cohort. The concordance index was used to assess the prognostic capability of the imaging signature (concordance index, 0–1). A concordance index of 1 indicates perfect prediction, and random guess gives a concordance index of 0.5. Kaplan-Meier analysis was used to estimate the probability of freedom from distant metastasis. The aforementioned optimal cutoff point from the discovery cohort was used to divide patients into high- or low-risk groups in the validation cohort. The statistical significance of concordance indexes and whether one concordance index was higher than another were assessed by means of bootstrapping. We used a bootstrap

Figure 1

without DM

SUVmax = 12.4
Volume = 16.1 mL
SUVpeak2mL = 4.9
Gauss_ClusterShade = 410.6

a.

with DM

SUVmax = 12.1
Volume = 12.1 mL
SUVpeak2mL = 8.2
Gauss_ClusterShade = 5510.2

b.

Figure 1: PET images in two patients with lung cancer whose tumors had similar SUV_{max} and tumor volume but different radiomic signatures. DM = distant metastasis. Arrows = tumor.

method with 50 subsamples and 100 repetitions from *(a)* original survival data and *(b)* permuted survival data or survival data in comparison, and then the concordance index distributions of *a* and *b* were analyzed by using the Wilcoxon signed-rank test. The statistical analysis was performed by using the R software.

Results

After removing highly correlated features (correlation coefficient > 0.95) and assessing their reproducibility (intraclass correlation coefficient > 0.8), 35 robust imaging features remained (see Table E1 [online]). On the basis of the discovery cohort, we used the optimal prognostic model to identify two radiomic features that allowed quantification of tumor texture and peak SUV. In particular, the texture feature was the cluster shade of the Gaussian filtered image within the Laws feature group (Gauss cluster shade),

and the other feature was the SUV corresponding to the top active 2 mL in the tumor volume ($SUV_{peak2mL}$). On the basis of the discovery cohort, the radiomic prognostic signature was defined as $2.1 \times SUV_{peak2mL} + 3.6 \times GCS$, where GCS is the Gauss cluster shade. Figure 1 shows two representative patients with and without distant metastasis whose tumors had similar SUV_{max} and tumor volume values, but had different radiomic signatures in terms of $SUV_{peak2mL}$ and Gauss cluster shade.

Figure 2 shows the Kaplan-Meier curves for predicting the risk of distant metastasis by using the proposed radiomic signature. In the discovery cohort, the radiomic signature achieved a concordance index of 0.73 ($P < .0001$) and a hazard ratio of 5.4 ($P = .0019$, log-rank test) for separating patients at low risk from those at high risk of distant metastasis. When tested in the independent validation cohort, the radiomic signature remained prognostic, with a concordance index of 0.71 (P

$< .0001$) and a hazard ratio of 4.8 ($P = .0498$, log-rank test). These results compared favorably ($P < .0001$) with conventional imaging metrics, where tumor volume had a concordance index of 0.64 ($P < .0001$) and a hazard ratio of 2.0 ($P = .54$, log-rank test), and SUV_{max} had a concordance index of 0.67 ($P < .0001$) and a hazard ratio of 1.5 ($P = .73$, log-rank test). For the whole population ($n = 101$), the proposed median imaging signature was 0.83 (interquartile range, 0.69–1.15) for patients without distant metastasis and 1.29 (interquartile range, 0.80–1.80) for patients with distant metastasis ($P = .02$, Wilcoxon test). The imaging features were normalized with z-scores. Neither tumor volume nor SUV_{max} was prognostic in the validation cohort, although SUV_{max} was prognostic in the discovery cohort (see Figs E1 and E2 [online]).

Finally, we combined the previously obtained radiomic signature with histologic type to build a prognostic model based on patients with known histologic results (adenocarcinoma vs squamous cell carcinoma). The combined radiomic-histologic signature was defined as $2.4 \times SUV_{peak2mL} + 4.2 \times GCS - 3.9 \times HT$, where GCS is the Gauss cluster shade and HT is the histologic type, with adenocarcinoma coded as 1 and squamous cell carcinoma coded as 0. Figure 3 shows the Kaplan-Meier curves for the composite model, which showed a significant separation between the high- and low-risk groups in both the discovery and validation cohorts. Also, the concordance index was increased to 0.80, indicating an improved predictive capability. A significant improvement ($P < .0001$) in predicting freedom from distant metastasis was seen when histologic information was added compared with a prognostic model based solely on imaging features. The concordance index obtained by using histologic type alone was merely 0.51 ($P = .77$). The prognostic capacity of the aforementioned models is summarized in Table 3.

Discussion

In this study, we identified prognostic PET imaging signatures in patients with
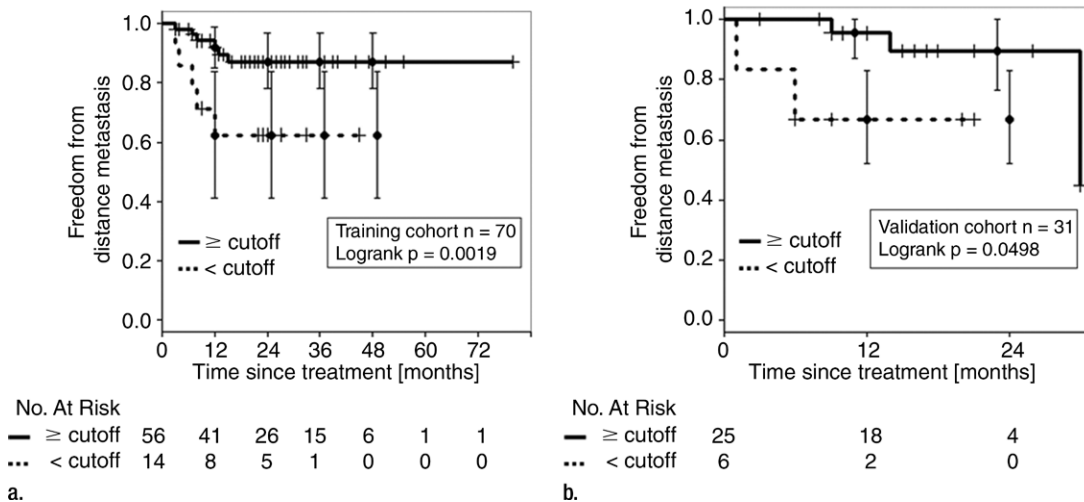
Figure 2

No. At Risk

— ≥ cutoff	56	41	26	15	6	1	1
⋯ < cutoff	14	8	5	1	0	0	0

a.

No. At Risk

— ≥ cutoff	25		18		4
⋯ < cutoff	6		2		0

b.

Figure 2: Kaplan-Meier curves of freedom from distant metastasis with proposed radiomic signature in **(a)** discovery cohort (*n* = 70) **(b)** and validation cohort (*n* = 31). Cutoff between patients at high and low risk was determined on the basis of discovery cohort and was fixed for validation cohort.
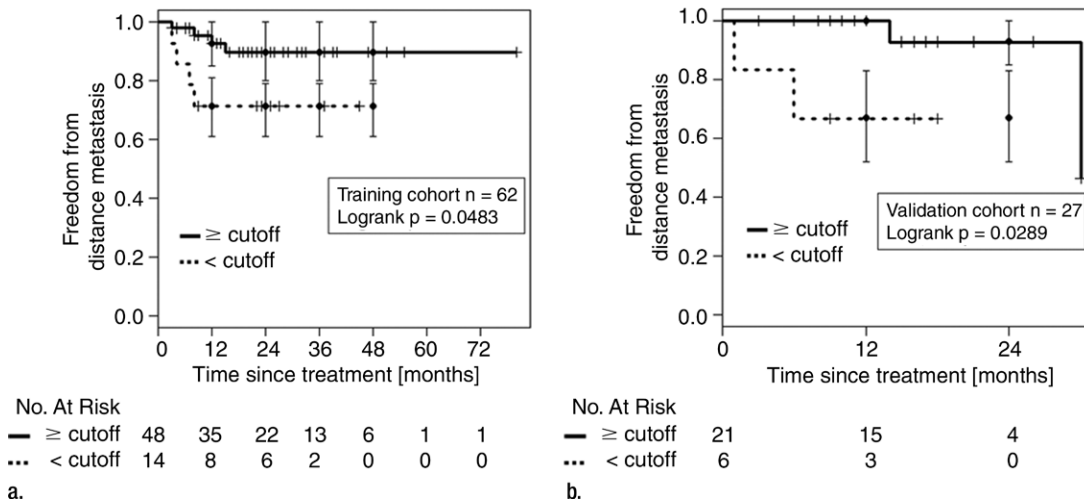
Figure 3

No. At Risk

— ≥ cutoff	48	35	22	13	6	1	1
⋯ < cutoff	14	8	6	2	0	0	0

a.

No. At Risk

— ≥ cutoff	21		15		4
⋯ < cutoff	6		3		0

b.

Figure 3: Kaplan-Meier curves of freedom from distant metastasis with combined radiomic-histologic signature in **(a)** discovery cohort (*n* = 62) **(b)** and validation cohort (*n* = 27). Cutoff between patients at high and low risk was determined on the basis of discovery cohort and was fixed for validation cohort.

early-stage NSCLC by using a quantitative radiomic approach. The imaging signature significantly improved the prognostic value compared with that of conventional imaging metrics. In addition, we found that combining imaging and histologic information yielded further improvement in predicting the risk of distant metastasis in patients with early-stage NSCLC. Another strength of our study was that we focused on patients with early-stage NSCLC only and identified predictors that stratify patients of similar clinical stages, whereas authors of many previous studies included patients of mixed stages and did not address specifically whether the predictors add important information beyond what was already known about the patient (eg, stage).

To the best of our knowledge, we are the first researchers to report on the investigation of quantitative FDG PET image features (ie, radiomics) for predicting distant metastasis in early-stage NSCLC after SABR. Authors of other recent studies (24,25) have addressed

Radiology

Table 3

Comparison of Three Prognostic Models for Predicting Distant Metastasis

Model and Covariate	Coefficient	P Value	Concordance Index*	P Value	Hazard Ratio
Univariate analysis of conventional predictors					
SUV$_{max}$	. . .	. . .	0.67 (0.22, 0.94)	<.0001	1.5
Volume	. . .	. . .	0.64 (0.20, 0.91)	<.0001	2.0
Histologic type	. . .	. . .	0.51 (0.15, 0.82)	.770	1.1
Multivariate analysis of radiomic signatures			0.71 (0.50, 0.92)	<.0001	4.8
SUV$_{peak2mL}$	2.1	.014			
Gauss cluster shade	3.6	.026			
Multivariate analysis of radiomic signatures combined with histologic type			0.80 (0.54, 1.00)	<.0001	6.9
SUV$_{peak2mL}$	2.4	.024			
Gauss cluster shade	4.2	.039			
Histologic type	−3.9	.047			

* Data in parentheses are 95% confidence intervals.

CT-based imaging features in locally advanced NSCLC. The patient population from our study (ie, early-stage NSCLC) is growing with the results of the national lung cancer screening trial (26) and recent financial support for screening programs by the Centers for Medicare and Medicaid Services (Decision Memo CAG-00439N, *www.cms.gov*). These results could have implications for patients who ultimately receive surgery or SABR, but are particularly pertinent for the patients who undergo SABR. Compared with patients who receive surgery, patients who undergo SABR are at greater risk of regional and distant metastasis, and many do not undergo lymph node evaluation at the time of treatment. Therefore, it will become increasingly important to identify patients who may benefit from adjuvant treatment, given risk of recurrence and increased life expectancy.

Intratumor heterogeneity has been suggested to correlate with worse patient outcome (27–33) and to manifest on multiple spatial scales (eg, at molecular or genetic, cellular, and tissue levels). In this study, the extraction of advanced PET imaging features allowed us to assess intratumor heterogeneity quantitatively on a macroscopic tissue scale. For predicting distant metastasis, one of the radiomic signatures (Laws feature) allowed quantification of regional heterogeneity of the PET image. Whether these macroscopic imaging features have clear underlying biologic relevance must be investigated further.

Our prognostic model combining histologic and imaging features (Table 3) suggests that, given similar radiomic signatures at PET, lung adenocarcinoma (coded as 0) tends to have a greater risk for distant metastasis than does squamous cell carcinoma (coded as 1). These results are consistent with those of a recent study (34) in which authors showed that, although lung squamous cell carcinomas tend to be more metabolically active with a higher SUV at FDG PET (generally a poor prognostic indicator), adenocarcinoma actually may have a higher metastatic potential than squamous cell carcinoma. On the other hand, the optimal imaging predictors of distant metastasis may be histologically specific. Therefore, in future prospective studies, developing a model of squamous cell carcinoma and adenocarcinoma separately may have greater clinical prognostic strength.

Given the tumor stage, certain concerns would arise regarding the stability and suitability of the proposed texture features. Authors of several previous articles (35,36) have investigated this issue, and, here, we addressed these concerns in two ways. First, we found that most of the patients from both the discovery and validation cohorts had a sufficient number of tumor voxels (>100 voxels) reconstructed on the original PET image. Moreover, the tumor voxel numbers of both cohorts are not significantly different (P = .34), with a median size in the discovery cohort of 412 voxels and in the validation cohort, 493 voxels. Next, we exhaustively tested the statistical difference of all the selected texture features between the large tumor group (≥ median tumor volume) and the small tumor group (< median tumor volume). Only four of 25 texture features (wavelet group 1 mean and entropy, wavelet group 2 mean, and Laws gradient cluster shade) were significantly different between the two groups, and more importantly, the texture feature (ie, Gauss cluster shade) that was finally chosen was relatively stable for both groups.

Our study had several limitations. This was a retrospective study with a relatively small cohort. The median follow-up time of 17 months is relatively short, considering that distant failures may occur up to several years after treatment. A technical limitation was respiratory motion during the three-dimensional PET acquisition, which may have led to distortion (mainly elongation and blurring) of the true metabolic activity, especially for tumors in the lower lobes of the lung. Respiratory-gated and four-dimensional PET acquisition (37) may help improve the quantitative accuracy of PET imaging.

For future studies, the prognostic models must be evaluated in large prospective cohorts with longer follow-up times. Considering the inherent variability in image acquisition protocol and reconstruction parameters, extensive multisite clinical validation is required before our radiomic signature can be translated into clinical practice. While glucose metabolic activity reflected on FDG PET images captures an important aspect of the underlying tumor biology, there may be other factors

such as the tumor microenvironment that also can influence clinical outcome (38). Combining FDG PET with other imaging modalities such as CT and with genomic signatures (39,40) may further improve the predictive value.

In conclusion, we have built models for predicting the risk of distant metastasis in early-stage NSCLC by combining quantitative PET imaging features and histologic information. These prognostic models must be validated further in prospective large cohorts. If successful, the proposed techniques may aid in identifying patients with NSCLC who would benefit from adjuvant therapy.

References

1. Timmerman R, Paulus R, Galvin J, et al. Stereotactic body radiation therapy for inoperable early stage lung cancer. JAMA 2010; 303(11):1070–1076.

2. Bradley JD, El Naqa I, Drzymala RE, Trovo M, Jones G, Denning MD. Stereotactic body radiation therapy for early-stage non-small-cell lung cancer: the pattern of failure is distant. Int J Radiat Oncol Biol Phys 2010;77(4): 1146–1150.

3. Pieterman RM, van Putten JW, Meuzelaar JJ, et al. Preoperative staging of non-small-cell lung cancer with positron-emission tomography. N Engl J Med 2000;343(4):254–261.

4. Machtay M, Duan F, Siegel BA, et al. Prediction of survival by [18F]fluorodeoxyglucose positron emission tomography in patients with locally advanced non-small-cell lung cancer undergoing definitive chemoradiation therapy: results of the ACRIN 6668/RTOG 0235 trial. J Clin Oncol 2013;31(30):3823–3830.

5. Nair VJ, MacRae R, Sirisegaram A, Pantarotto JR. Pretreatment [18F]-fluoro-2-deoxyglucose positron emission tomography maximum standardized uptake value as predictor of distant metastasis in early-stage non-small cell lung cancer treated with definitive radiation therapy: rethinking the role of positron emission tomography in personalizing treatment based on risk status. Int J Radiat Oncol Biol Phys 2014;88(2):312–318.

6. Satoh Y, Onishi H, Nambu A, Araki T. Volume-based parameters measured by using FDG PET/CT in patients with stage I NSCLC treated with stereotactic body radiation therapy: prognostic value. Radiology 2014;270(1):275–281.

7. Meng X, Sun X, Mu D, et al. Noninvasive evaluation of microscopic tumor extensions using standardized uptake value and metabolic tumor volume in non-small-cell lung cancer. Int J Radiat Oncol Biol Phys 2012;82(2):960–966.

8. Liao S, Penney BC, Wroblewski K, et al. Prognostic value of metabolic tumor burden on 18F-FDG PET in nonsurgical patients with non-small cell lung cancer. Eur J Nucl Med Mol Imaging 2012;39(1):27–38.

9. Abelson JA, Murphy JD, Trakul N, et al. Metabolic imaging metrics correlate with survival in early stage lung cancer treated with stereotactic ablative radiotherapy. Lung Cancer 2012;78(3):219–224.

10. Kumar V, Gu Y, Basu S, et al. Radiomics: the process and the challenges. Magn Reson Imaging 2012;30(9):1234–1248.

11. Depeursinge A, Yanagawa M, Leung AN, Rubin DL. Predicting adenocarcinoma recurrence using computational texture models of nodule components in lung CT. Med Phys 2015;42(4):2054–2063. [Published correction appears in Med Phys 2015;42(5):2653.]

12. Aerts HJ, Velazquez ER, Leijenaar RT, et al. Decoding tumour phenotype by noninvasive imaging using a quantitative radiomics approach. Nat Commun 2014;5:4006.

13. Hatt M, Majdoub M, Vallières M, et al. 18F-FDG PET uptake characterization through texture analysis: investigating the complementary nature of heterogeneity and functional tumor volume in a multi-cancer site patient cohort. J Nucl Med 2015;56(1):38–44.

14. Fried DV, Mawlawi O, Zhang L, et al. Stage III non-small cell lung cancer: prognostic value of FDG PET quantitative imaging features combined with clinical prognostic factors. Radiology 2016;278(1):214–222.

15. Haralick RM, Shanmugam K, Dinstein IH. Textural features for image classification. IEEE Trans Syst Man Cybern 1973;SMC-3(6):610–621.

16. Mallat SG. A theory for multiresolution signal decomposition: the wavelet representation. IEEE Trans Pattern Anal Mach Intell 1989;11(7):674–693.

17. Laws KI. Rapid texture identification. 24th annual technical symposium: International Society for Optics and Photonics, 1980; 376–381.

18. Chuang KS, Tzeng HL, Chen S, Wu J, Chen TJ. Fuzzy c-means clustering with spatial information for image segmentation. Comput Med Imaging Graph 2006;30(1):9–15.

19. Tibshirani R. Regression shrinkage and selection via the lasso. J R Stat Soc Series B Stat Methodol 1996;58(1):267–288.

20. Friedman J, Hastie T, Tibshirani R. Regularization paths for generalized linear models via coordinate descent. J Stat Softw 2010; 33(1):1–22.

21. Walters SJ. What is a Cox model? Newmarket, England: Hayward Medical Communications, 1999.

22. Budczies J, Klauschen F, Sinn BV, et al. Cutoff Finder: a comprehensive and straightforward Web application enabling rapid biomarker cutoff optimization. PLoS One 2012;7(12): e51862.

23. Therneau TM. A Package for Survival Analysis in R. R package version 2.38-3. http://CRAN.R-project.org/package=survival Accessed July 15, 2015.

24. Coroller TP, Grossmann P, Hou Y, et al. CT-based radiomic signature predicts distant metastasis in lung adenocarcinoma. Radiother Oncol 2015;114(3):345–350.

25. Fried DV, Tucker SL, Zhou S, et al. Prognostic value and reproducibility of pretreatment CT texture features in stage III non-small cell lung cancer. International Journal of Radiation Oncology Biology Physics. 2014; 90(4):834-42.

26. National Lung Screening Trial Research Team, Aberle DR, Adams AM, et al. Reduced lung-cancer mortality with low-dose computed tomographic screening. N Engl J Med 2011;365(5):395–409.

27. Tixier F, Le Rest CC, Hatt M, et al. Intratumor heterogeneity characterized by textural features on baseline 18F-FDG PET images predicts response to concomitant radiochemotherapy in esophageal cancer. J Nucl Med 2011;52(3):369–378.

28. Ganeshan B, Panayiotou E, Burnand K, Dizdarevic S, Miles K. Tumour heterogeneity in

non-small cell lung carcinoma assessed by CT texture analysis: a potential marker of survival. Eur Radiol 2012;22(4):796–802.

29. Win T, Miles KA, Janes SM, et al. Tumor heterogeneity and permeability as measured on the CT component of PET/CT predict survival in patients with non-small cell lung cancer. Clin Cancer Res 2013;19(13):3591–3599.

30. Cook GJ, O'Brien ME, Siddique M, et al. Non-small cell lung cancer treated with erlotinib: heterogeneity of (18)F-FDG uptake at PET-association with treatment response and prognosis. Radiology 2015;276(3):883–893.

31. Tixier F, Hatt M, Valla C, et al. Visual versus quantitative assessment of intratumor 18F-FDG PET uptake heterogeneity: prognostic value in non-small cell lung cancer. J Nucl Med 2014;55(8):1235–1241.

32. Cook GJ, Yip C, Siddique M, et al. Are pretreatment 18F-FDG PET tumor textural features in non-small cell lung cancer associ-

ated with response and survival after chemoradiotherapy? J Nucl Med 2013;54(1): 19–26.

33. El Naqa I, Grigsby P, Apte A, et al. Exploring feature-based approaches in PET images for predicting cancer treatment outcomes. Pattern Recognit 2009;42(6):1162–1171.

34. Schuurbiers OC, Meijer TW, Kaanders JH, et al. Glucose metabolism in NSCLC is histology-specific and diverges the prognostic potential of 18FDG-PET for adenocarcinoma and squamous cell carcinoma. J Thorac Oncol 2014;9(10):1485–1493.

35. Brooks FJ, Grigsby PW. The effect of small tumor volumes on studies of intratumoral heterogeneity of tracer uptake. J Nucl Med 2014;55(1):37–42.

36. Hatt M, Cheze-le Rest C, van Baardwijk A, Lambin P, Pradier O, Visvikis D. Impact of tumor size and tracer uptake heterogeneity in (18)F-FDG PET and CT non-small cell

lung cancer tumor delineation. J Nucl Med 2011;52(11):1690–1697.

37. Nehmeh SA, Erdi YE, Pan T, et al. Four-dimensional (4D) PET/CT imaging of the thorax. Med Phys 2004;31(12):3179–3186.

38. Gentles AJ, Bratman SV, Lee LJ, et al. Integrating tumor and stromal gene expression signatures with clinical indices for survival stratification of early-stage non-small cell lung cancer. J Natl Cancer Inst 2015;107(10).

39. Nair VS, Gevaert O, Davidzon G, et al. Prognostic PET 18F-FDG uptake imaging features are associated with major oncogenomic alterations in patients with resected non-small cell lung cancer. Cancer Res 2012;72(15): 3725–3734.

40. Gevaert O, Xu J, Hoang CD, et al. Non-small cell lung cancer: identifying prognostic imaging biomarkers by leveraging public gene expression microarray data--methods and preliminary results. Radiology 2012;264(2):387–396.